

Sensitivity Analysis of Fracture Scattering

by

Xinding Fang

B.S. Geophysics

University of Science and Technology of China, 2008

SUBMITTED TO THE DEPARTMENT OF EARTH, ATMOSPHERIC, AND PLANETARY
SCIENCES IN PARTIAL FULFILLMENT OF THE REQUIREMENTS FOR THE DEGREE
OF

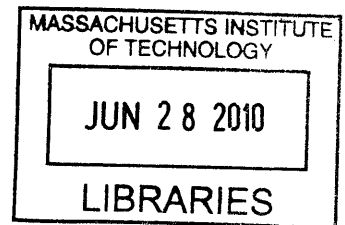
MASTER OF SCIENCE IN GEOPHYSICS
AT THE
MASSACHUSETTS INSTITUTE OF TECHNOLOGY

June 2010

© Massachusetts Institute of Technology, 2010. All rights reserved.

The author hereby grants to MIT permission to reproduce
and distribute publicly paper and electronic
copies of the thesis document in whole or in part
in any medium now known or hereafter created.

ARCHIVES



Author
Department of Earth, Atmospheric, and Planetary Sciences
May 14, 2010

Certified by
Michael Fehler
Senior Research Scientist-Earth Resources Laboratory
Thesis Supervisor

Accepted by
Maria T. Zuber
Head of the Department of Earth, Atmospheric, and Planetary Sciences

Sensitivity Analysis of Fracture Scattering

by

Xinding Fang

Submitted to the Department of Earth, Atmospheric, and Planetary Science
on May 21, 2010, in partial fulfillment of the requirements
for the degree of Master of Science in Geophysics

Abstract

We use a 2-D finite difference method to numerically calculate the seismic response of a single finite fracture in a homogeneous media. In our experiments, we use a point explosive source and ignore the free surface effect, so the fracture scattering wave field contains two parts: P-to-P scattering and P-to-S scattering. We vary the fracture compliance within a range considered appropriate for field observations, 10^{-12} m/Pa to 10^{-9} m/Pa, and investigate the variation of the scattering pattern of a single fracture as a function of normal and tangential fracture compliance. We show that P-to-P and P-to-S fracture scattering patterns are sensitive to the ratio of normal to tangential fracture compliance and different incident angle, while radiation pattern amplitudes scale as the square of the compliance. We find that, for a vertical fracture system, if the source is located at the surface, most of the energy scattered by a fracture propagates downwards, specifically, the P-to-P scattering energy propagates down and forward while the P-to-S scattering energy propagates down and backward. Therefore, most of the fracture scattered waves observed on the surface are, first scattered by fractures, and then reflected back to the surface by reflectors below the fracture zone, so the fracture scattered waves have complex ray paths and are contaminated by the reflectivity of matrix reflectors.

Thesis Supervisor: Michael Fehler

Title: Senior Research Scientist – Earth Resources Laboratory

Acknowledgements

I would like to thank many people for their help towards the completion of this thesis during my two years of studying in the Earth Resource Laboratory at MIT.

First of all, I would like to thank my thesis advisor, Dr. Michael Fehler for his support and guidance throughout my study at MIT. I always feel lucky to meet and work with such a reputable scientist as Dr. Fehler who offered me the chance to enter MIT as well as the field of geophysics. I would also like to thank Dr. Daniel Burns for his fruitful suggestions regarding my current as well as future work.

I would like to acknowledge the Fracture group (Michael Fehler, Dan Burns, Zhenya Zhu, Tianrun Chen, Stephen Brown, and Sudish Bakku) for many helpful comments and exposure to different aspects of the fracture problem during our weekly meetings.

This work was funded by the Eni Multiscale Reservoir Science Project within the Eni-MIT Energy Initiative Founding Member Program.

Contents

Chapter 1. Introduction	5
Chapter 2. Finite-difference Modeling Method	8
2.1 Linear Slip Fracture Model	8
2.2 Effective Medium Theory	10
2.3 Discussion on the Fracture Compliance Value	14
Chapter 3. Sensitivity Analysis of Fracture Scattering	18
3.1 Methodology	18
3.2 Numerical Results & Discussions	22
3.2.1 Fracture scattering pattern as a function of compliance	24
3.2.2 Scattering strength	31
3.2.3 The effect of matrix Poisson's ratio on fracture scattering pattern	35
3.2.4 The effect of fracture length on fracture scattering	36
3.3 Suggestions on Field Data Processing	37
Chapter 4. Conclusions	39
Bibliography	40

Chapter 1

Introduction

Fractures are common within the subsurface and play a critical role in the mechanical and fluid flow properties of earth materials. In regions where the maximum compressive stress is vertical, open fractures will tend to be vertical and oriented perpendicular to the minimum horizontal stress direction. The ability to interpret properties such as fracture spacing, orientation, compliance, and fluid content associated with such fracture systems is vital to the effective extraction and management of reservoir resources, such as oil and gas and geothermal reservoirs, and the monitoring of contaminant migration and CO₂ injection. Therefore, it is critical to detect and characterize fracture networks for optimal development and production of carbonate reservoirs.

The detection of reservoir fractures using seismic methods has been traditionally based on effective medium theories that assume fractures in a rock mass are much smaller than the wavelengths and are distributed throughout the rock. Fractures can also be modeled as discrete inclusions in the medium. The linear slip deformation theory (Schoenberg, 1980) is particularly fit to study the discrete effects of fractures as it expresses a single fracture as a displacement discontinuity, the magnitude of the displacement jump being related to the specific fracture compliance. This theory predicts a frequency dependent seismic response

and agrees with experimental observations of wave propagation through fractured rocks (Pyrak-Nolte et al., 1987).

Schoenberg's approach has also been used to model the complicated phenomena that occur in the presence of multiple parallel fracture sets including seismic scattering and wave guiding (e.g. Daley et al., 2002). By analyzing some of these types of fracture models, Willis et al. (2006), developed a novel and practical technique to characterize fractures at the reservoir level known as the Scattering Index Method.

When fractures are small relative to the seismic wavelength, waves will be weakly affected by fractures, and in effective medium theory, this fracture zone is equivalent to a homogeneous anisotropic zone without fracture (Hudson, 1991; Coates and Schoenberg, 1995; Schoenberg and Sayers, 1995; Grechka and Kachanov, 2006; Grechka, 2007; Sayers, 2009). When fractures are much larger than the seismic wavelength, then we can take fracture interfaces as infinite planes and apply plane wave theory to calculate their reflection and transmission coefficients and interface waves (Schoenberg, 1980; Pyrak-Nolte and Cook, 1987; Gu et al., 1996). In field reservoirs, fractures always have finite length, and fractures with characteristic lengths on the order of seismic wavelength are one of the important scattering sources that generate seismic codas. Sanchez-Sesma and Iturraran-Viveros (2001) derived an approximate analytical solution of scattering and diffraction of SH waves by a finite fracture, and Chen (submitted to SEG 2010) derived an analytical solution for scattering from a 2D elliptical crack in an isotropic acoustic medium. However, so far it is still too difficult to derive the

analytical elastic solution of a finite fracture with a linear-slip boundary and characteristic length on the order of the seismic wavelength. Although fractures are usually present as fracture networks in reservoirs, and the interaction between fracture networks and seismic waves is very complicated, single scattering can be considered as the 1st order effect on the scattered wave field. Therefore, to study the general elastic response of single finite fracture is essential to reservoir fracture characterization, and this has been done numerically.

Chapter 2

Finite-difference Modeling Method

In this Chapter, first we will give a brief introduction to Schoenberg's linear slip fracture model, and then, by combining Schoenberg's model and the effective medium theory, we will talk about some details of the finite-difference modeling method.

2.1 Linear Slip Fracture Model (Schoenberg, 1980)

Displacements are, generally, discontinuous across fracture surfaces S_q , the strains are singular at S_q . Thus, the strain field in a solid with fractures is a sum of regular and singular parts:

$$\varepsilon_{ij} = s_{ijkl}^b \sigma_{kl} + \frac{1}{2} \sum_q ([u_i]n_j + [u_j]n_i)_q \delta(S_q) \quad (2.1.1)$$

where, in representing the regular part as $s_{ijkl}^b \sigma_{kl}$, the matrix material is assumed to be linear elastic (with compliance tensor s_{ijkl}^b) and $\delta(S_q)$ is a delta function concentrated on S_q (it has the dimension of length^{-1}). Displacement discontinuity vector $[\vec{u}] = \vec{u}^+ - \vec{u}^-$ (crack opening displacement) and unit normal \vec{n} are, generally, variable along fractures; their directions are coordinated by defining the "+" side of S as corresponding to the positive sense of \vec{n} (then change of sign of \vec{n} changes the sign of $[\vec{u}]$ and the products $[\vec{u}]\vec{n}$, $\vec{n}[\vec{u}]$ remain invariant).

The representation of the extra strain due to the cracks and fractures in the form of the second

term in equation (2.1.1) directly follows from the general representation of average ε_{ij} in terms of boundary displacements. Such representations have been used in the literature since the early 1970s (for details and review, see Kachanov [1992]).

We assume the matrix material to be elastically homogeneous: $s_{ijkl}^b(\vec{x}) = \text{const} = s_{ijkl}^0$.

Averaging (2.1.1) over V and using the property of $\delta(S)$ that $\int_V f(x)\delta(S)dV$ reduces to the surface integral $\int_S f(x)dS$ yields the volume average of strain:

$$\begin{aligned}\langle \varepsilon_{ij} \rangle &= s_{ijkl}^0 \langle \sigma_{kl} \rangle + \frac{1}{2V} \sum_q \int_{S_q} ([u_i]n_j + [u_j]n_i) dS \\ &= (s_{ijkl}^0 + \Delta s_{ijkl}) \langle \sigma_{kl} \rangle \equiv s_{ijkl} \langle \sigma_{kl} \rangle\end{aligned}\quad (2.1.2)$$

where Δs_{ijkl} is the change in compliance due to fractures and s_{ijkl} is the effective compliance. Linear dependence of $[\vec{u}]$ on $\langle \sigma_{kl} \rangle$ assumes linear elasticity of the matrix and absence of friction on the crack. Note that equation (2.1.2) is applicable to finite nonplanar fractures in the long wavelength limit, i.e., the applied stress is assumed to be constant over the representative volume V .

In the following, we omit the averaging signs $\langle \rangle$ for stresses and strains, assuming $\varepsilon_{ij} \equiv \langle \varepsilon_{ij} \rangle$ and $\sigma_{ij} \equiv \langle \sigma_{ij} \rangle$.

Assume fracture interactions may be neglected so that $[\vec{u}]$ is determined by σ_{ij} . This assumption is exact for a set of infinite flat parallel fractures subject to a uniform stress field. Note that this assumption of noninteraction does not imply that the excess compliance as a result of the fractures is small relative to the unfractured background compliance.

When the fractures are approximately planar and parallel, and their unit normal is denoted by

n_i , a linearity assumption is conveniently introduced through a “fracture system compliance tensor” Z with Z_{ij} such that,

$$\frac{1}{V} \sum_q \int_{S_q} [u_i] dS \equiv Z_{ij} \sigma_{jk} n_k \quad (2.1.3)$$

where Z_{ij} is symmetric and nonnegative definite.

Let the extra strain as a result of the fractures be $s_{ijkl}^f \sigma_{kl}$ ($s_{ijkl}^f = \Delta s_{ijkl}$ is the change in compliance due to fractures), so that s_{ijkl}^f may be thought of as an excess compliance tensor as a result of the presence of the parallel fractures. Substitution of equation (2.1.3) into equation (2.1.2) yields,

$$\begin{aligned} s_{ijkl}^f \sigma_{kl} &= \frac{1}{2} (Z_{ir} \sigma_{rs} n_s n_j + Z_{jr} \sigma_{rs} n_s n_i) \\ &= \frac{1}{2} (Z_{ir} n_s n_j + Z_{jr} n_s n_i) \frac{\delta_{rk} \delta_{sl} + \delta_{rl} \delta_{sk}}{2} \sigma_{kl} \end{aligned} \quad (2.1.4)$$

So one obtains,

$$s_{ijkl}^f = \frac{1}{4} (Z_{ik} n_j n_l + Z_{jk} n_i n_l + Z_{il} n_j n_k + Z_{jl} n_i n_k) \quad (2.1.5)$$

2.2 Effective Medium Theory

Rotationally Invariant Fracture Sets

The simplest assumption concerning Z_{ij} is to let the normal compliance of the fractures be given by Z_N and the tangential compliance by Z_T . This causes the fracture behavior to be invariant with respect to rotation about an axis normal to the fractures under this condition,

$$\begin{aligned} Z_{ij} &= Z_N n_i n_j + Z_T (\delta_{ij} - n_i n_j) \\ &= Z_T \delta_{ij} + (Z_N - Z_T) n_i n_j \end{aligned} \quad (2.2.1)$$

So that the excess compliance tensor of a single rotationally invariant fracture set becomes,

$$s_{ijkl}^f = \frac{1}{4}Z_T(\delta_{ik}n_jn_l + \delta_{jk}n_in_l + \delta_{il}n_jn_k + \delta_{jl}n_in_k) + (Z_N - Z_T)n_in_jn_kn_l \quad (2.2.2)$$

Consider a single set of rotationally invariant vertical fractures whose normal is parallel to the x_I -axis, i.e., $n_I=(1, 0, 0)$. In this case,

$$\begin{aligned} s_{1111}^f &= Z_N, \\ s_{1212}^f &= s_{2121}^f = s_{1221}^f = s_{2112}^f = s_{1313}^f = s_{3131}^f = s_{1331}^f = s_{3113}^f = \frac{Z_T}{4} \end{aligned} \quad (2.2.3)$$

with all other compliance components equal to zero. In conventional (2-subscript) condensed 6 x 6 matrix notation, 11->1, 22->2, 33->3, 23->4, 13->5, 12->6, while factors 2 and 4 are introduced as follows:

$$s_{ijkl} \rightarrow S_{pq} \quad \text{when both } p, q \text{ are } 1, 2, \text{ or } 3;$$

$$2s_{ijkl} \rightarrow S_{pq} \quad \text{when one of } p, q \text{ are } 4, 5, \text{ or } 6;$$

$$4s_{ijkl} \rightarrow S_{pq} \quad \text{when both } p, q \text{ are } 4, 5, \text{ or } 6.$$

These factors of 2 or 4 are absent in the condensation of the stiffness tensor components. Thus the excess compliance may be written in the following 6 x 6 matrix form:

$$S^f = \begin{bmatrix} Z_N & 0 & 0 & 0 & 0 & 0 \\ 0 & 0 & 0 & 0 & 0 & 0 \\ 0 & 0 & 0 & 0 & 0 & 0 \\ 0 & 0 & 0 & 0 & 0 & 0 \\ 0 & 0 & 0 & 0 & Z_T & 0 \\ 0 & 0 & 0 & 0 & 0 & Z_T \end{bmatrix} \quad (2.2.4)$$

For a single set of rotationally invariant fractures in an isotropic background, the medium is transversely isotropic (TI) with its symmetry axis perpendicular to the fractures. This is, however, a restricted subset of all possible TI media since it depends only on the two background moduli, say Lamé parameters μ and λ , and two nonnegative fracture compliance

Z_N and Z_T . The total 6 x 6 compliance matrix of this TI medium whose symmetry axis is parallel to the x_1 direction is given by

$$S = S^b + S^f \quad (2.2.5)$$

$$= \begin{bmatrix} \frac{\lambda + \mu}{\mu(3\lambda + 2\mu)} + Z_N & -\frac{\lambda}{2\mu(3\lambda + 2\mu)} & -\frac{\lambda}{2\mu(3\lambda + 2\mu)} & & & \\ -\frac{\lambda}{2\mu(3\lambda + 2\mu)} & \frac{\lambda + \mu}{\mu(3\lambda + 2\mu)} & -\frac{\lambda}{2\mu(3\lambda + 2\mu)} & & & \\ -\frac{\lambda}{2\mu(3\lambda + 2\mu)} & -\frac{\lambda}{2\mu(3\lambda + 2\mu)} & \frac{\lambda + \mu}{\mu(3\lambda + 2\mu)} & & & \\ & & & \frac{1}{\mu} & & \\ & & & & \frac{1}{\mu} + Z_T & \\ & & & & & \frac{1}{\mu} + Z_T \end{bmatrix}$$

In finite-difference modeling, the whole model is discretized into small grid cells, and each grid cell is taken as a single effective unit, the effective fracture compliance for one cell is given as

$$\tilde{Z}_{ij} = \frac{1}{L} Z_{ij} \quad (2.2.6)$$

where

$$\frac{1}{L} = \frac{\Delta a}{\Delta V} \quad (2.2.7)$$

Δa is the area of the fracture plane lying within the cell volume and ΔV is the volume of the cell.

Thus, in numerical modeling, we only need to replace the fracture compliance with the effective fracture compliance (2.2.6), for convenience, hereafter, Z_{ij} will represent the effective fracture compliance.

Inverting equation (2.2.5) yields the elastic stiffness matrix,

$$C = \begin{bmatrix} M_b(1-\delta_N) & \lambda(1-\delta_N) & \lambda(1-\delta_N) \\ \lambda(1-\delta_N) & M_b(1-r_b^2\delta_N) & \lambda(1-r_b\delta_N) \\ \lambda(1-\delta_N) & \lambda(1-r_b\delta_N) & M_b(1-r_b^2\delta_N) \\ & & & \mu \\ & & & & \mu(1-\delta_T) \\ & & & & & \mu(1-\delta_T) \end{bmatrix} \quad (2.2.8)$$

where

$$M_b = \lambda + 2\mu, \quad r_b = \frac{\lambda}{M_b} = \frac{\nu}{1-\nu}$$

$$0 \leq \delta_T = \frac{Z_T\mu}{1+Z_T\mu} < 1, \quad 0 \leq \delta_N = \frac{Z_N M_b}{1+Z_N M_b} < 1.$$

If the fracture normal is not parallel to x_1 , then we need to rotate stiffness tensor (2.2.8) back to the global coordinate.

Assume local and global Cartesian coordinates are (x, y, z) and (x', y', z') , rotation matrix is

$$\beta_{ij} = \cos \left\{ \begin{bmatrix} x' \\ y' \\ z' \end{bmatrix} \begin{bmatrix} x & y & z \end{bmatrix} \right\} \quad (2.2.9)$$

then, the stress and stiffness tensor in global coordinate are

$$\sigma'_{ij} = \beta_{ik}\beta_{jl}\sigma_{kl} \quad (2.2.10)$$

$$c'_{ijkl} = \beta_{ip}\beta_{jq}\beta_{kr}\beta_{ls}c_{pqrs} \quad (2.2.11)$$

If the stiffness and compliance tensors are expressed in 6 by 6 matrix notation, we can use

Bond transformation matrices for coordinate transformation, the global stiffness and

compliance tensors in condensed format can be expressed as

$$C' = M \cdot C \cdot M^T \quad (2.2.12)$$

$$S' = N \cdot S \cdot N^T \quad (2.2.13)$$

M and N are Bond transformation matrices. The elements of the 6×6 M and N matrices are

given in terms of the direction cosines as follows:

$$M = \begin{bmatrix} \beta_{11}^2 & \beta_{12}^2 & \beta_{13}^2 & 2\beta_{12}\beta_{13} & 2\beta_{13}\beta_{11} & 2\beta_{11}\beta_{12} \\ \beta_{21}^2 & \beta_{22}^2 & \beta_{23}^2 & 2\beta_{22}\beta_{23} & 2\beta_{23}\beta_{21} & 2\beta_{21}\beta_{22} \\ \beta_{31}^2 & \beta_{32}^2 & \beta_{33}^2 & 2\beta_{32}\beta_{33} & 2\beta_{33}\beta_{31} & 2\beta_{31}\beta_{32} \\ \beta_{21}\beta_{31} & \beta_{22}\beta_{32} & \beta_{23}\beta_{33} & \beta_{22}\beta_{33} + \beta_{23}\beta_{32} & \beta_{21}\beta_{33} + \beta_{23}\beta_{31} & \beta_{22}\beta_{31} + \beta_{21}\beta_{32} \\ \beta_{31}\beta_{11} & \beta_{32}\beta_{12} & \beta_{33}\beta_{13} & \beta_{12}\beta_{33} + \beta_{13}\beta_{32} & \beta_{11}\beta_{33} + \beta_{13}\beta_{31} & \beta_{11}\beta_{32} + \beta_{12}\beta_{31} \\ \beta_{11}\beta_{21} & \beta_{12}\beta_{22} & \beta_{13}\beta_{23} & \beta_{22}\beta_{13} + \beta_{12}\beta_{23} & \beta_{11}\beta_{23} + \beta_{13}\beta_{21} & \beta_{22}\beta_{11} + \beta_{12}\beta_{21} \end{bmatrix} \quad (2.2.14)$$

$N =$

$$\begin{bmatrix} \beta_{11}^2 & \beta_{12}^2 & \beta_{13}^2 & \beta_{12}\beta_{13} & \beta_{13}\beta_{11} & \beta_{11}\beta_{12} \\ \beta_{21}^2 & \beta_{22}^2 & \beta_{23}^2 & \beta_{22}\beta_{23} & \beta_{23}\beta_{21} & \beta_{21}\beta_{22} \\ \beta_{31}^2 & \beta_{32}^2 & \beta_{33}^2 & \beta_{32}\beta_{33} & \beta_{33}\beta_{31} & \beta_{31}\beta_{32} \\ 2\beta_{21}\beta_{31} & 2\beta_{22}\beta_{32} & 2\beta_{23}\beta_{33} & \beta_{22}\beta_{33} + \beta_{23}\beta_{32} & \beta_{21}\beta_{33} + \beta_{23}\beta_{31} & \beta_{22}\beta_{31} + \beta_{21}\beta_{32} \\ 2\beta_{31}\beta_{11} & 2\beta_{32}\beta_{12} & 2\beta_{33}\beta_{13} & \beta_{12}\beta_{33} + \beta_{13}\beta_{32} & \beta_{11}\beta_{33} + \beta_{13}\beta_{31} & \beta_{11}\beta_{32} + \beta_{12}\beta_{31} \\ 2\beta_{11}\beta_{21} & 2\beta_{12}\beta_{22} & 2\beta_{13}\beta_{23} & \beta_{22}\beta_{13} + \beta_{12}\beta_{23} & \beta_{11}\beta_{23} + \beta_{13}\beta_{21} & \beta_{22}\beta_{11} + \beta_{12}\beta_{21} \end{bmatrix} \quad (2.2.15)$$

2.3 Discussion on the Fracture Compliance Value

There is still uncertainty about the appropriate value of fracture compliance of reservoir fractures. Because fracture scattering is the second order effect on seismic data, and fracture scattered waves that can be observed in the field are contaminated by the scattering of background heterogeneities and the waves reflected from the structure, so it is very hard to measure the compliance of fractures in reservoirs directly. Laboratory measurement of fractured rock samples is an easier way to get some ideas on the value of fracture compliance. Pyrak-Nolte and Morris (1999) measured values of $10^{-11} - 10^{-13}$ m/Pa for a suite of granitic samples with single fractures. Pyrak-Nolte et al. (1990) and Worthington et al. (2007) found values of $10^{-12} - 10^{-14}$ m/Pa for single fractures in quartz monzonite and limestone,

respectively. Measurements of fracture compliance in small-scale near surface experiments using acoustic logs (Lubbe and Worthington, 2006), VSP (Hardin et al., 1987), and cross hole measurements (Myer et al., 1997) found values of $10^{-11} - 10^{-13}$ m/Pa for single fractures.

Laboratory measurements of fractured rock samples suggest that the fracture compliance values are small. Reservoir scale estimates of fracture compliance, however, suggest that values could be up to 10^{-9} m/Pa for seismic scale fractures. One study (Worthington and Hudson, 2000), based on the estimation of seismic attenuation from VSP data acquired through a large fault/fracture zone in a North sea well, found that transmission losses through a zone containing 5 fractures with compliance values of 10^{-9} m/Pa explained the data extremely well.

Compliance measurements are summarized in Table 2.3.1 (Worthington, 2007) and in Figure 2.3.1. All of these data suggest that the range of fracture compliance is very large ($10^{-14} - 10^{-9}$ m/Pa), and the implication is that fracture compliance increases with increasing scale. In numerical modeling of reservoir with layer structure and fractures, waves reflected from the structure are usually stronger than the fracture scattered waves, and they make it difficult to see the fracture scattered waves if we use a value of fracture compliance smaller than 10^{-10} m/Pa. Thus, in order to obtain the scattered wave field that is comparable to the scattering of reservoir scale fracture, we usually use fracture compliance values of $10^{-10} - 10^{-9}$ m/Pa for our numerical simulations.

The normal to tangential fracture compliance ratio is also a very important parameter for fracture characterization, because this ratio is a strong function of the way the fracture surfaces interact. This ratio contains the information about the material filling the fracture, and determining it may be of use for fluid identification. Both numerical simulations (Sayers, 2009; Gurevich, 2009) and laboratory measurements (Lubbe, 2008; Gurevich, 2009) suggest that the compliance ratio Z_N/Z_T should be less than 1. Based on laboratory experiment data, Lubbe (2008) suggested that a Z_N/Z_T ratio of 0.5 is a representative value to use in modeling studies of gas filled fractures, and the compliance ratio can be less than 0.1 for fluid saturated fractures.

NO.	Normal Compliance Z_n (m/Pa)	Tangential Compliance Z_t (m/Pa)	Measured Method	Reference
1	$10^{-12} - 10^{-14}$	$10^{-13} - 10^{-14}$	Laboratory	Pyrak-Nolte et al (1990)
2	$2*10^{-14}$	$2*10^{-14}$	Laboratory	Worthington et al (2007)
3	$10^{-13} - 4*10^{-13}$		VSP	Hardin et al (1987)
4	$0.25*10^{-12} - 3.5*10^{-12}$		Sonic log	Lubbe&Worthington (2006)
5	$2*10^{-12}$		Cross hole	Myer et al (1997)
6		10^{-9}	VSP	Worthington&Hudson (2000)

Table 2.3.1: Summary of fracture compliance values from lab and field measurements (taken from Worthington (2007)).

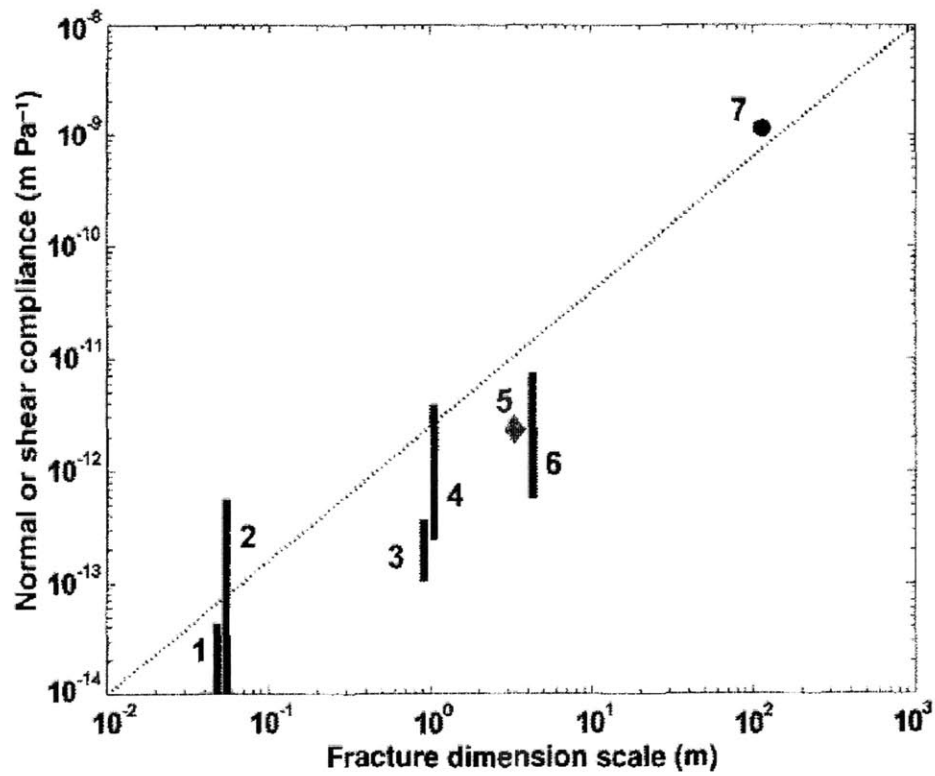


Figure 2.3.1: Summary of fracture compliance versus scale for the lab and field measurements in Table 2.3.1. Taken from Worthington (2007).

Chapter 3

Sensitivity Analysis of Fracture Scattering

In this Chapter, first we will discuss the methodology for calculating the seismic response of scattering from a single fracture, and then we will show the scattering patterns and scattering strength of a single fracture for many different models. Our modeling is all conducted limited in 2D.

3.1 Methodology

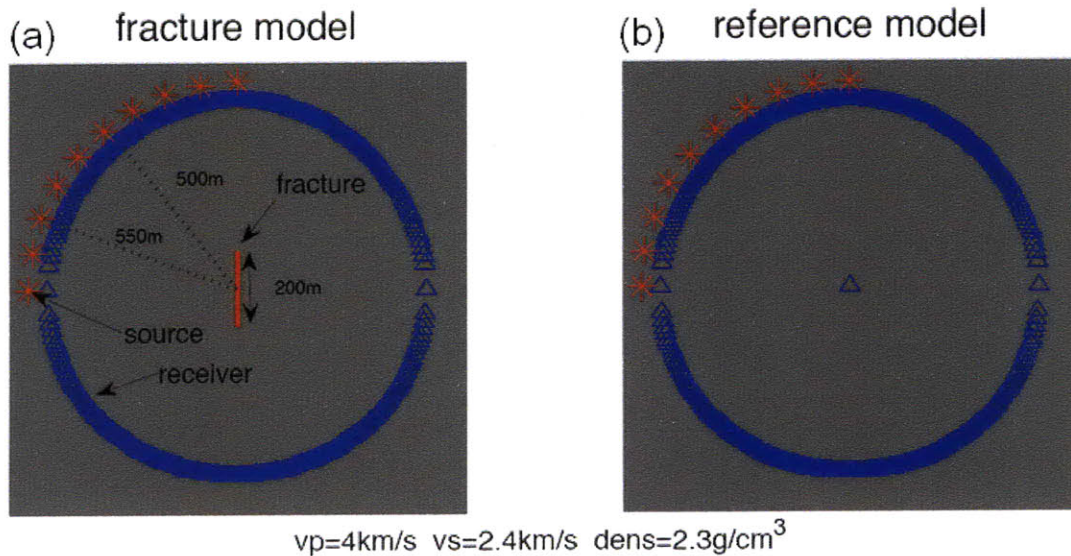


Figure 3.1.1: (a) is the fracture model and (b) is the reference model, these two models are exactly the same except for the presence of a fracture in (a) indicated by the red line. Blue triangles are receivers and they are equidistant from the fracture center, red asterisks indicate sources at different angle of incidence to the fracture. Incident angles are measured from the normal of the fracture (e.g. a source directly above the fracture is considered to have a 90° incident angle).

We assume the whole wave field recorded at receivers in the fracture model (1a) is $\vec{u}(\vec{r}, t, \theta_{\text{inc}})$, and the corresponding wave field recorded in the reference model (1b) is $\vec{u}_0(\vec{r}, t, \theta_{\text{inc}})$, then

$$\vec{u}(\vec{r}, t, \theta_{\text{inc}}) = \vec{u}_0(\vec{r}, t, \theta_{\text{inc}}) + \vec{s}(\vec{r}, t, \theta_{\text{inc}}) \quad (3.1.1)$$

where $\vec{s}(\vec{r}, t, \theta_{\text{inc}})$ is the scattered wave field, θ_{inc} is the incident angle.

In the frequency domain, equation (3.1.1) can be written as

$$\vec{U}(\vec{r}, \omega, \theta_{\text{inc}}) = \vec{U}_0(\vec{r}, \omega, \theta_{\text{inc}}) + \vec{S}(\vec{r}, \omega, \theta_{\text{inc}}) \quad (3.1.2)$$

where \vec{U} , \vec{U}_0 and \vec{S} are the Fourier transformations of \vec{u} , \vec{u}_0 and \vec{s} , respectively, and ω is angular frequency.

Thus, the scattered wave field can be expressed as

$$\vec{S}(\vec{r}, \omega, \theta_{\text{inc}}) = \vec{U}(\vec{r}, \omega, \theta_{\text{inc}}) - \vec{U}_0(\vec{r}, \omega, \theta_{\text{inc}}) \quad (3.1.3)$$

We assume the source is a pressure point source and we ignore the Earth's free surface, so the scattered wave field $\vec{S}(\vec{r}, \omega, \theta_{\text{inc}})$ includes two parts: P-to-P scattered wave field $\vec{S}_{\text{pp}}(\vec{r}, \omega, \theta_{\text{inc}})$ and P-to-S scattered wave field $\vec{S}_{\text{ps}}(\vec{r}, \omega, \theta_{\text{inc}})$.

In homogeneous isotropic media, the wave equation in the frequency domain can be expressed as

$$\vec{U}(\vec{r}, \omega) = -\left(\frac{V_p}{\omega}\right)^2 \nabla[\nabla \cdot \vec{U}(\vec{r}, \omega)] + \left(\frac{V_s}{\omega}\right)^2 \nabla \times [\nabla \times \vec{U}(\vec{r}, \omega)] \quad (3.1.4)$$

where V_p and V_s are P- and S-wave velocity.

In homogeneous isotropic media, we can separate the P- and S-wave energy by simply calculating the divergence and curl of the whole displacement field, thus, equation (3.1.4) can be written as

$$\vec{U}(\vec{r}, \omega, \theta_{\text{inc}}) = \vec{U}_p(\vec{r}, \omega, \theta_{\text{inc}}) + \vec{U}_s(\vec{r}, \omega, \theta_{\text{inc}}) \quad (3.1.5)$$

with

$$\vec{U}_p(\vec{r}, \omega, \theta_{\text{inc}}) = -\left(\frac{v_p}{\omega}\right)^2 \nabla[\nabla \cdot \vec{U}(\vec{r}, \omega, \theta_{\text{inc}})] \text{ is the P-wave displacement,} \quad (3.1.5a)$$

$$\vec{U}_s(\vec{r}, \omega, \theta_{\text{inc}}) = \left(\frac{v_s}{\omega}\right)^2 \nabla \times [\nabla \times \vec{U}(\vec{r}, \omega, \theta_{\text{inc}})] \text{ is the S-wave displacement.} \quad (3.1.5b)$$

therefore,

$$\vec{S}(\vec{r}, \omega, \theta_{\text{inc}}) = \vec{S}_{pp}(\vec{r}, \omega, \theta_{\text{inc}}) + \vec{S}_{ps}(\vec{r}, \omega, \theta_{\text{inc}}) \quad (3.1.6)$$

$$\vec{S}_{pp}(\vec{r}, \omega, \theta_{\text{inc}}) = \vec{U}_p(\vec{r}, \omega, \theta_{\text{inc}}) - \vec{U}_0(\vec{r}, \omega, \theta_{\text{inc}}) \quad (3.1.7)$$

$$\vec{S}_{ps}(\vec{r}, \omega, \theta_{\text{inc}}) = \vec{U}_s(\vec{r}, \omega, \theta_{\text{inc}}) \quad (3.1.8)$$

Note that $\vec{U}_0(\vec{r}, \omega, \theta_{\text{inc}})$ is the reference wave field, and it has no S-wave component.

$\vec{S}_{pp}(\vec{r}, \omega, \theta_{\text{inc}})$ and $\vec{S}_{ps}(\vec{r}, \omega, \theta_{\text{inc}})$ are frequency dependent, and we wish to obtain the fracture response function which is independent of the source pulse used in modeling.

Thus, we write

$$|\vec{S}_{pp}(\vec{r}, \omega, \theta_{\text{inc}})| = a \cdot F_{pp}(\theta, \omega, \theta_{\text{inc}}) \cdot |\vec{I}(\omega, \theta_{\text{inc}})| \quad (3.1.9)$$

$$|\vec{S}_{ps}(\vec{r}, \omega, \theta_{\text{inc}})| = a \cdot F_{ps}(\theta, \omega, \theta_{\text{inc}}) \cdot |\vec{I}(\omega, \theta_{\text{inc}})| \quad (3.1.10)$$

with

$$a = \begin{cases} 1/\sqrt{r} & \text{for 2D} \\ 1/r & \text{for 3D} \end{cases} \quad (3.1.11)$$

where $F_{pp}(\theta, \omega, \theta_{\text{inc}})$ and $F_{ps}(\theta, \omega, \theta_{\text{inc}})$ are P-to-P and P-to-S fracture response functions, respectively, a is the geometrical spreading factor which is a function of the distance (r) from the receiver to the fracture center, and $\vec{I}(\omega, \theta_{\text{inc}})$ is the incident wave field recorded at the center of the fracture, θ and θ_{inc} are scattering angle and incident angle. Since the wave field is recorded at receivers that are equi-distance from the fracture center, and we only look at the far field scattering, so we can replace \vec{r} by θ in F_{pp} and F_{ps} . Because $\vec{I}(\omega, \theta_{\text{inc}})$ is the

incident wave field recorded at the center of the fracture, while $\vec{S}_{pp}(\vec{r}, \omega)$ and $\vec{S}_{ps}(\vec{r}, \omega)$ are the scattered wave fields recorded at a certain distance away from the center of the fracture, as shown in figure 3.1.1b, so we need to add the geometrical spreading factor a in equations (3.1.9) and (3.1.10). Usually, we will fix θ_{inc} when we calculate F_{pp} and F_{ps} for a given θ_{inc} , thus, for the sake of convenience, hereafter F_{pp} and F_{ps} will only be expressed as functions of θ and ω , but they depend on the incident angle.

In general, $F_{pp}(\theta, \omega)$ and $F_{ps}(\theta, \omega)$ are 2nd rank tensors, but it is difficult to describe the fracture response quantitatively by a 2nd rank tensor, because it contains 6 independent components. Therefore, for the sake of convenience, we assume $F_{pp}(\theta, \omega)$ and $F_{ps}(\theta, \omega)$ are scalars, and they represent the frequency-dependent response of a finite fracture.

The fracture response function $F_{pp}(\theta, \omega)$ and $F_{ps}(\theta, \omega)$ can be expressed as

$$F_{pp}(\theta, \omega) = \frac{|\vec{U}_p(\vec{r}, \omega, \theta_{inc}) - \vec{U}_0(\vec{r}, \omega, \theta_{inc})|}{a|\vec{I}(\omega, \theta_{inc})|} \quad (3.1.12)$$

$$F_{ps}(\theta, \omega) = \frac{|\vec{U}_s(\vec{r}, \omega, \theta_{inc})|}{a|\vec{I}(\omega, \theta_{inc})|} \quad (3.1.13)$$

Here, we emphasize that fracture response functions (3.1.12) and (3.1.13) are frequency dependent but are source-wavelet independent, we can get the same answer even though we use different source wavelets to calculate (3.1.12) and (3.1.13) numerically. $F_{pp}(\theta, \omega)$ and $F_{ps}(\theta, \omega)$ are functions of frequency, radiation angle, incident angle, matrix velocity, fracture compliance and wave-length to fracture-length ratio, and we can get the scattering radiation pattern by plotting them in polar coordinate.

3.2 Numerical Results & Discussions

From the comparison of many numerical results we find that, for a given incident angle, if we only consider the fracture response function as a function of fracture compliances (keep other conditions, such as background medium, fracture length, etc., unchanged), then the fracture scattering pattern is dominated by the compliance ratio γ ($\gamma=Z_N/Z_T$), and the scattering strength is affected by the magnitude of Z_N and Z_T .

For demonstrating the source wavelet independence of the fracture response function, we use two Ricker source wavelets with different central frequencies (20Hz and 40Hz) to calculate the radiation pattern of a single fracture. As shown in figure 3.2.1, these four figures are the radiation patterns of a fracture with normal and tangential compliance equal to 10^{-10} m/Pa, figures 3.2.1a and 3.2.1c show the same P-to-P fracture scattering pattern, but they are obtained individually by using two Ricker sources with 20Hz and 40Hz central frequency, respectively, figures 3.2.1b and 3.2.1d show the corresponding P-to-S fracture scattering patterns. Although we only show the case of 50^0 incidence, based on many numerical examples we can find that both P-to-P and P-to-S scattering patterns are independent of source center frequency regardless the varying of incident angle and fracture compliances, which proves the reliability of equations (3.1.12) and (3.1.13).

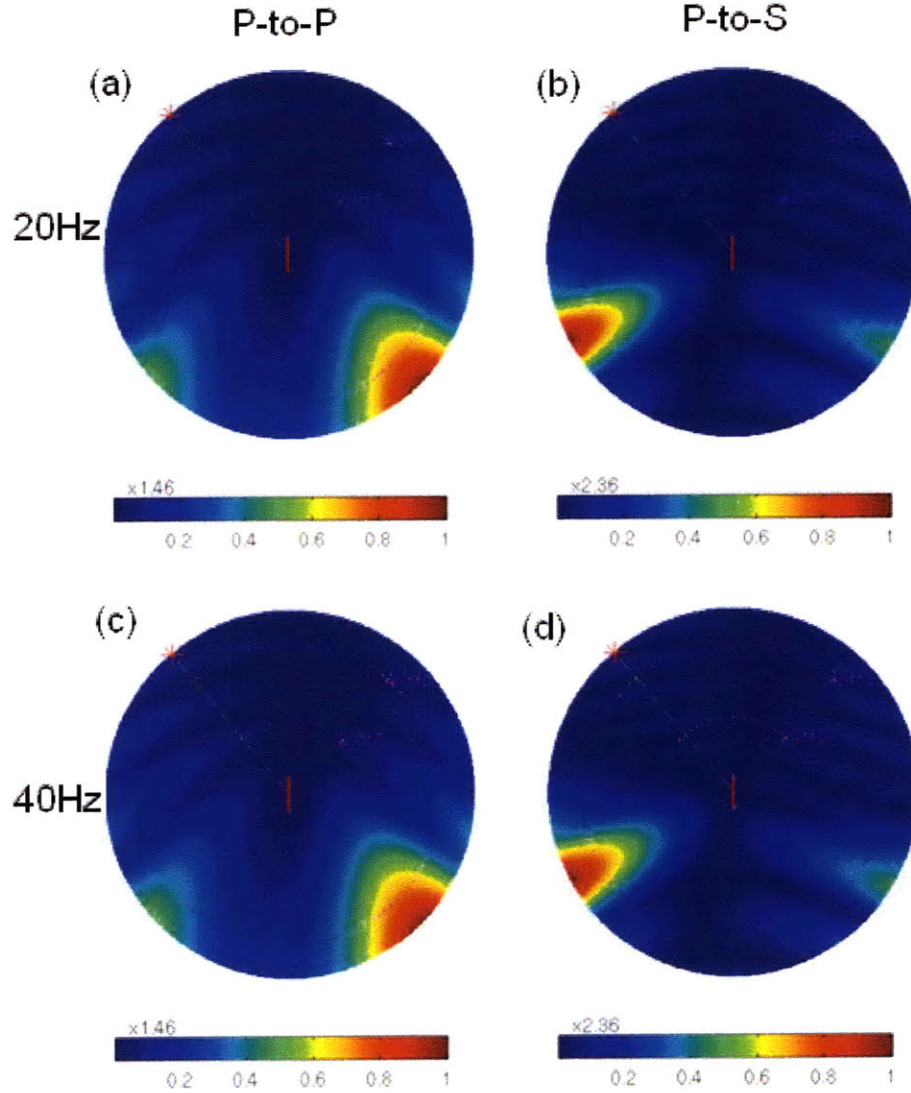
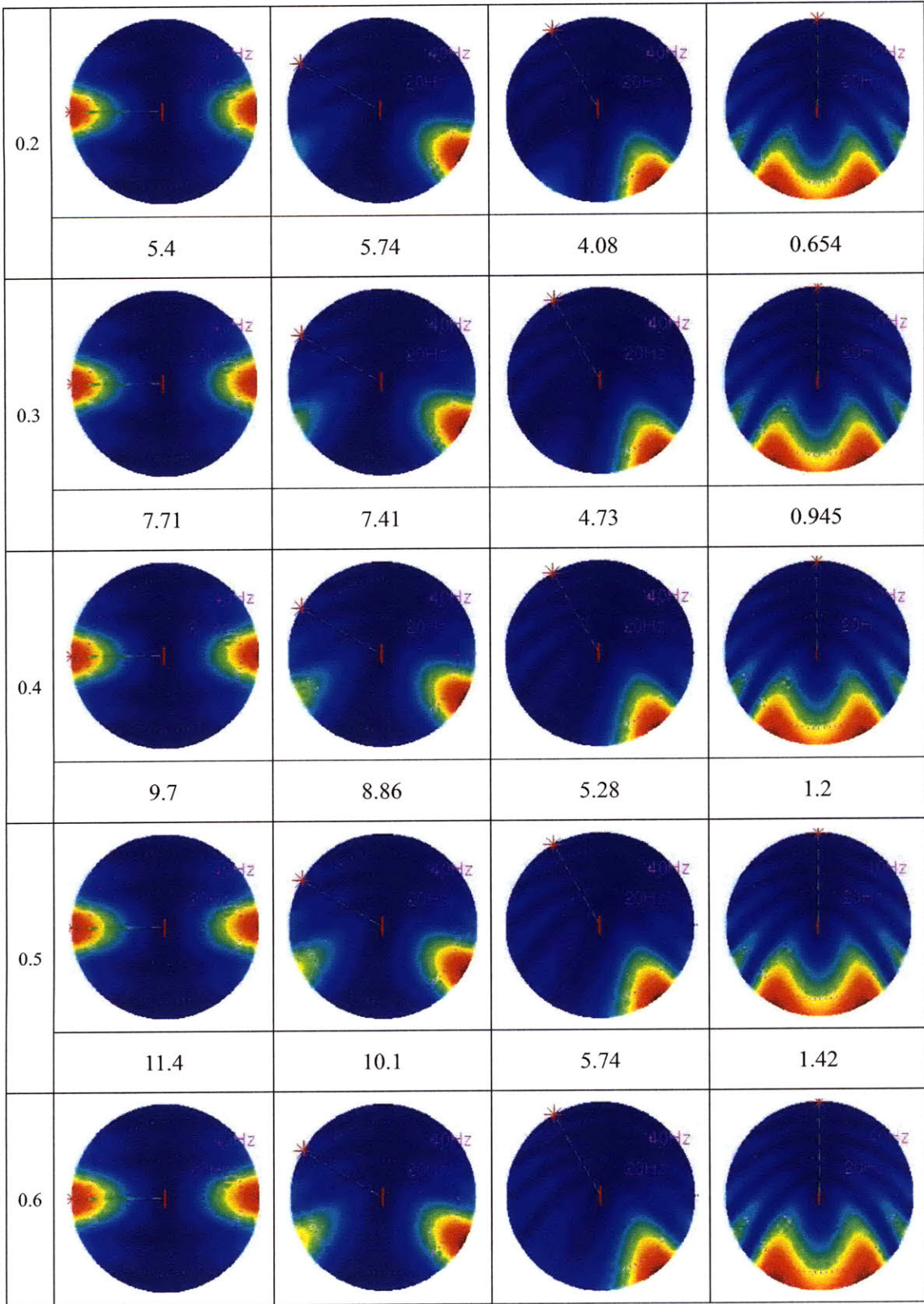


Figure 3.2.1: $F_{pp}(\theta, \omega)$ (a and c) and $F_{ps}(\theta, \omega)$ (b and d) of a fracture with normal and tangential compliance equal to 10^{-10} m/Pa. The radial and angular coordinates are $\omega/(2\pi)$ and θ . The source central frequency for figures 3.2.1a and 3.2.1b is 20Hz, while the source central frequency for figures 3.2.1c and 3.2.1d is 40Hz. The red line indicates a finite fracture with 200m length, and the red asteroid indicates the source position, the incident angle is 50° to the normal of the fracture. Here and after, the fracture response function is normalized in plotting, and the number above the colorbar is the scaled factor.

3.2.1 Fracture scattering pattern as a function of compliance.

Table 3.2.1 shows the P-to-P fracture response functions for fracture having ten different compliance ratios at four different incident angles. We define back scattering and forward scattering with respect to the fracture plane, in our numerical examples, the scattering at the left side of the fracture plane, where the source is located, is defined as back scattering, and the scattering at the opposite side of the fracture plane is defined as forward scattering. P-to-P fracture scattering patterns are nearly independent of compliance ratios when the incident angle is close to 0^0 or 90^0 , while P-to-P back scattering changes significantly with intermediate incidence angles. Table 3.2.2 shows the corresponding P-to-S fracture scattering patterns. P-to-S scattering patterns do not vary too much except for small angles of incidence, and in most cases P-to-S back scattering is much stronger than P-to-S forward scattering. For both P-to-P and P-to-S scattering, the scattering strength increases with increasing compliance magnitude, and the scattering pattern will not change if the compliance ratio does not change.

θ_{inc} γ	0^0	30^0	60^0	90^0
0.1				
	2.82	3.89	3.37	0.335



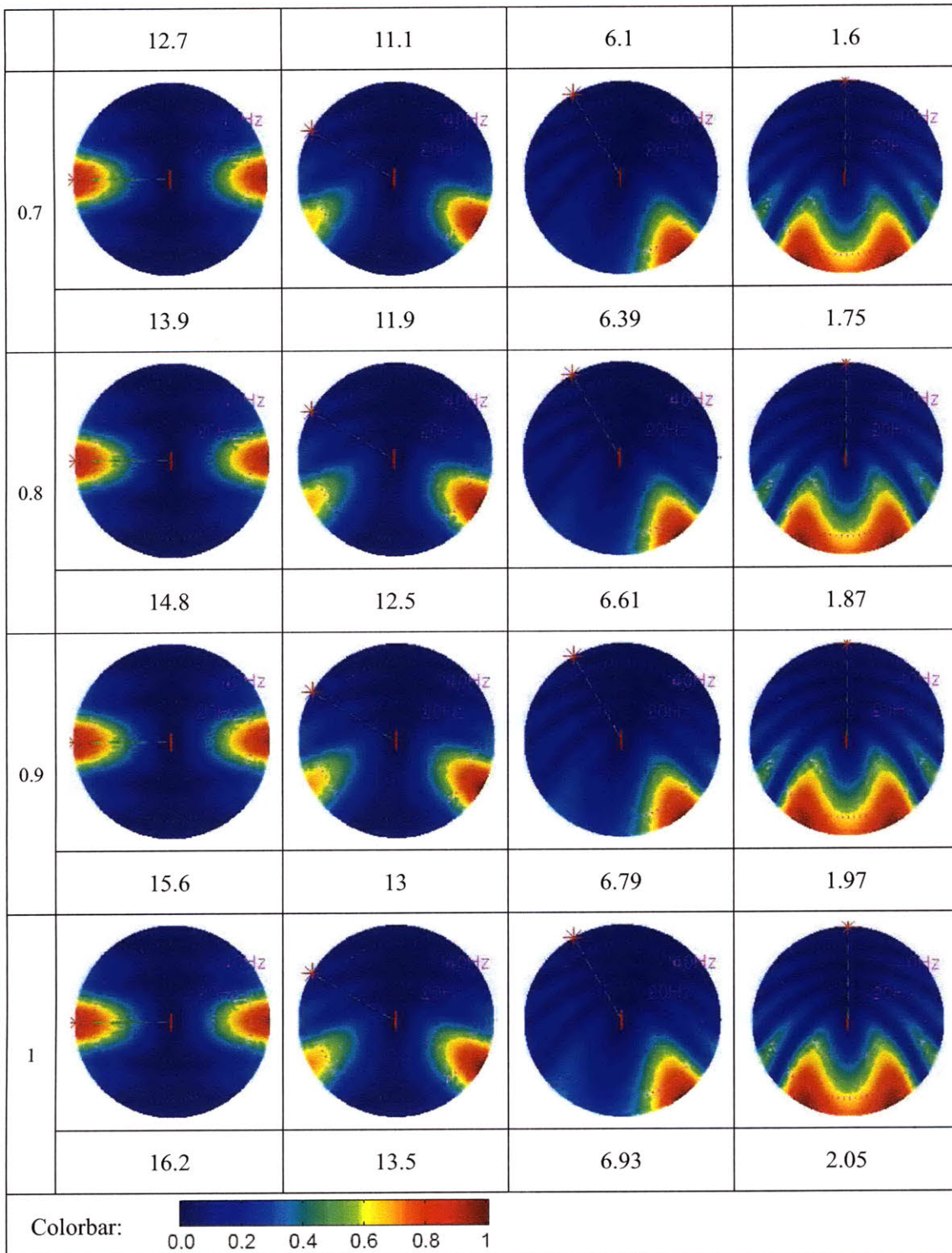
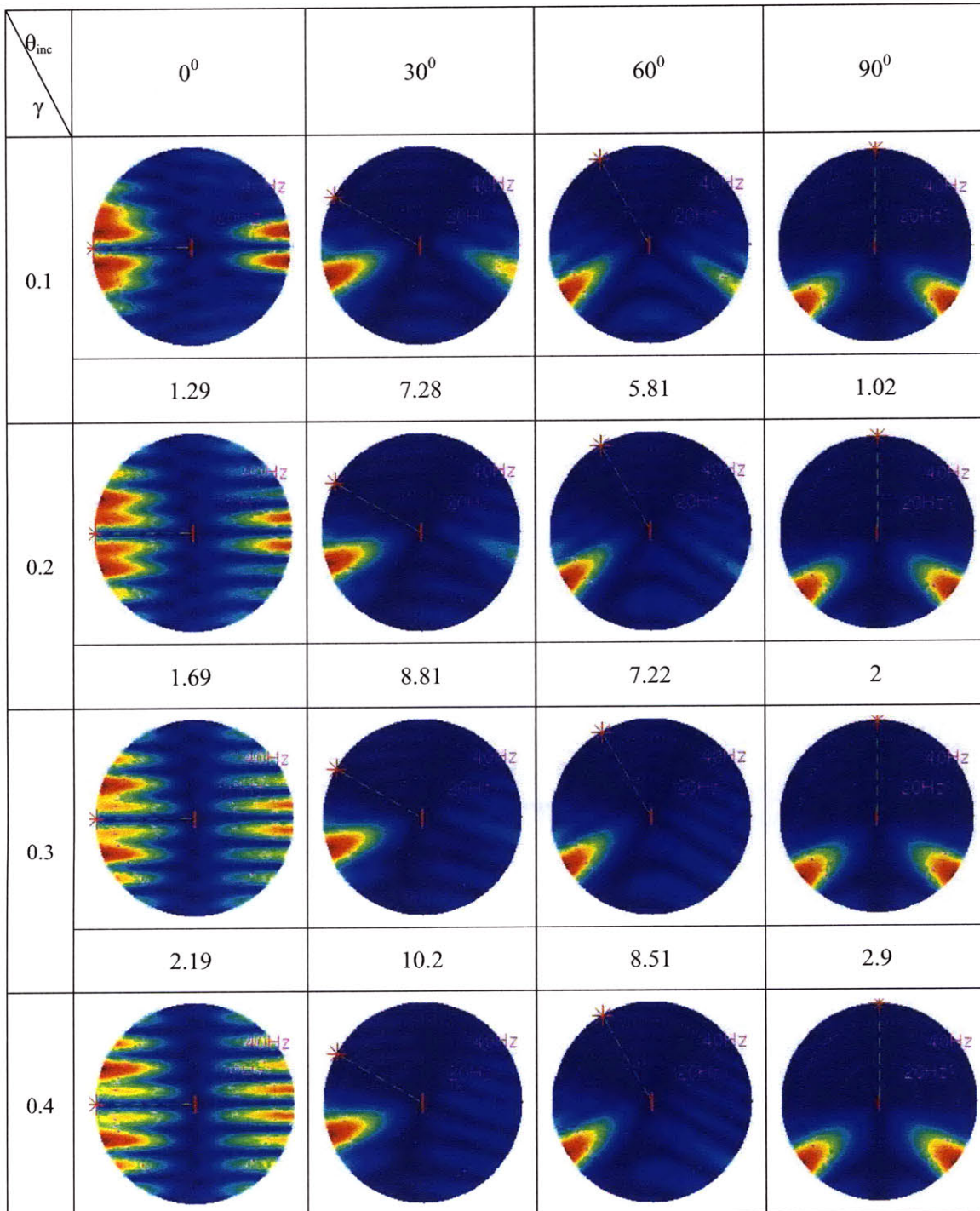
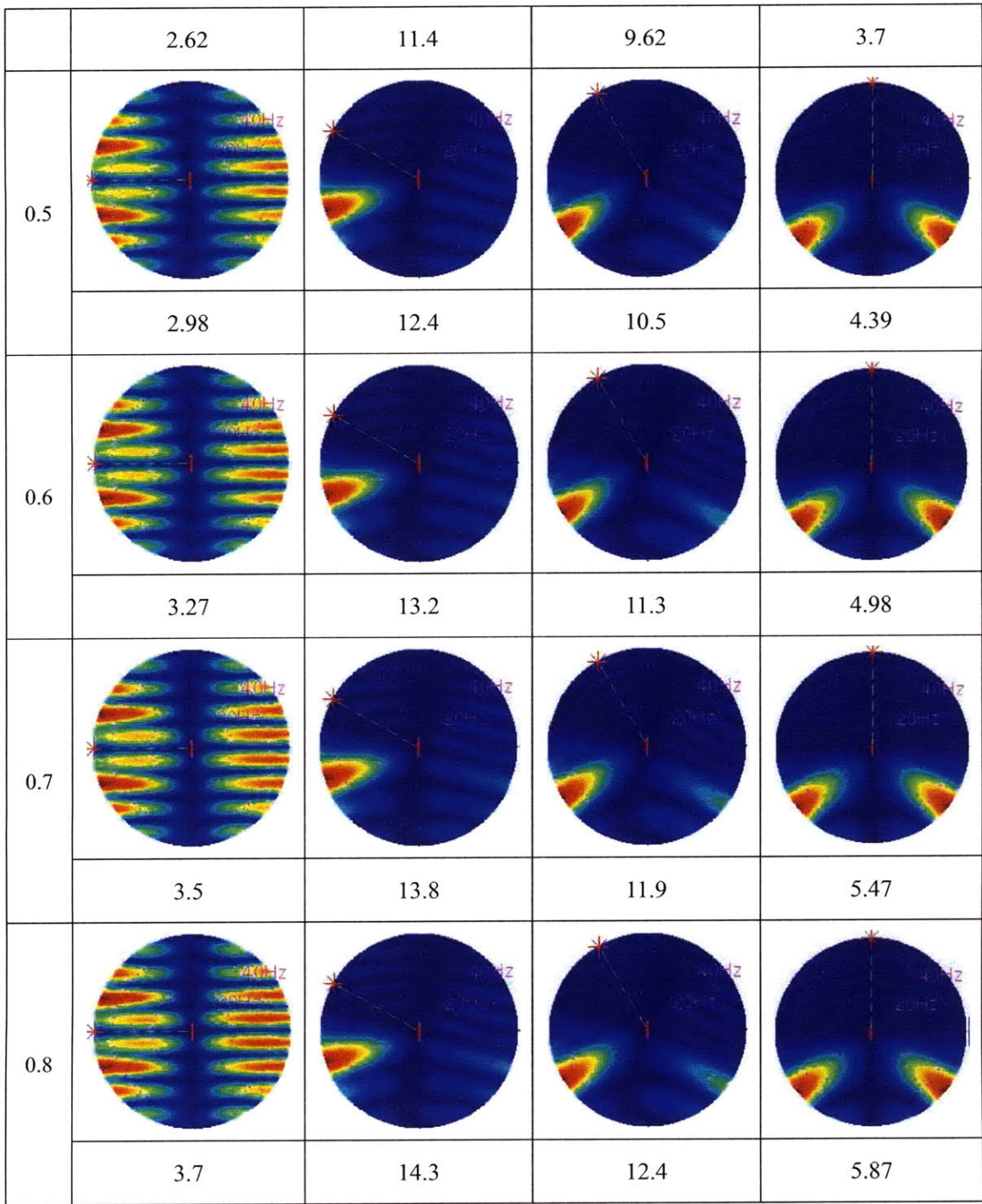


Table 3.2.1: $F_{pp}(\theta, \omega)$ for different compliance ratio γ and different incident angles are plotted in polar coordinates, the radial and angular coordinates are $\omega/(2\pi)$ and θ . The range of $\omega/(2\pi)$ in each panel is from 0Hz to 50Hz. Incident angles, which are shown on top of the figure, are 0° , 30° , 60° and 90° for each column. The compliance ratio for each row is shown at the left side

of each row. The number below each panel is the scaled factor in plotting and denotes the maximum scattering strength. Tangential compliance is fixed to 10^{-9} m/Pa, normal compliance varies. Fracture length is 200m, matrix P-wave and S-wave velocities are 4 km/s and 2.4 km/s, density is 2.3 g/cm^3 .





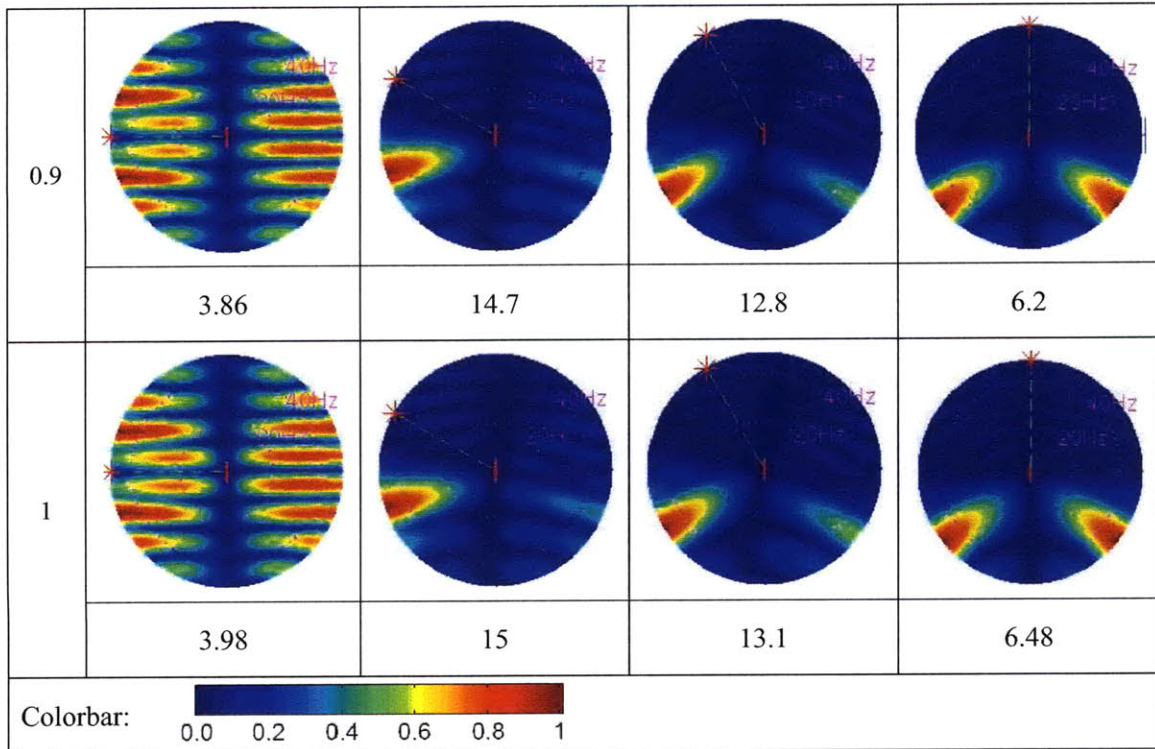


Table 3.2.2: $F_{ps}(\theta, \omega)$ for different compliance ratio γ and different incident angles are plotted in polar coordinates, the radial and angular coordinates are $\omega/(2\pi)$ and θ .

From Tables 3.2.1 and 3.2.2, we can find that, when the incident angle is between 0° and 90° , for P-to-P scattering, forward scattering is much stronger than back scattering, however, for P-to-S scattering, back scattering is much stronger than forward scattering. Moreover, most of the scattering energy propagates downwards if the fracture is close to vertical and the source is above the fracture. Specifically, the P-to-P scattering energy propagates down and forward (away from the source) while the P-to-S scattering energy propagates down and backward (towards the source). In the field, most fractures are close to vertical and the source is on the surface. In this case, the seismic waves first will be diffracted by fracture tips, and then most of the scattering energy will propagate downward, and then it will be reflected back to the surface by reflectors below the fracture zone, as illustrated in figure 3.2.1.

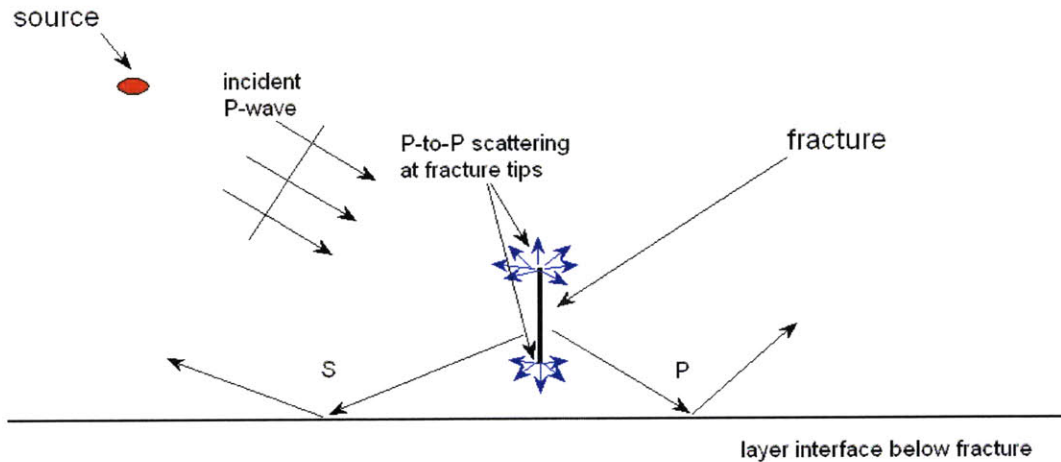


Figure 3.2.1: Cartoon showing how incident P-waves are scattered by a fracture. Scattering energy includes three parts: (i) P-to-P scattering at fracture tips; (ii) P-to-P forward scattering; (iii) P-to-S back scattering.

Figure 3.2.2 shows a numerical simulation of wave propagation in a uniform medium containing 21 non-parallel fractures, 3.2.2a shows the geometry of the model, 3.2.2b and 3.2.2c show snapshots of the divergent field and curl field of the scattered wave field at 0.54s (the scattered wave field is obtained by subtracting the whole wave field from the reference wave field of the same model without fractures). We can see that most of the P-to-P scattered energy is going down and forward and most of the P-to-S scattered energy is going down and backward. Therefore, most scattered signals observed on the surface come from fracture tips and reflectors below the fracture zone. We can only see fracture tips if we use traditional migration methods to search for fractures. In order to image subsurface fractures, we need to develop statistical methods to analyze the fracture scattered signals, and the scattering index method (Willis, 2006) is one of these methods. Also, if we want to use both P-to-P and P-to-S scattered waves to study fractures, we should search for P-to-P and P-to-S scattered waves at ‘forward’ and ‘backward’ receivers separately.

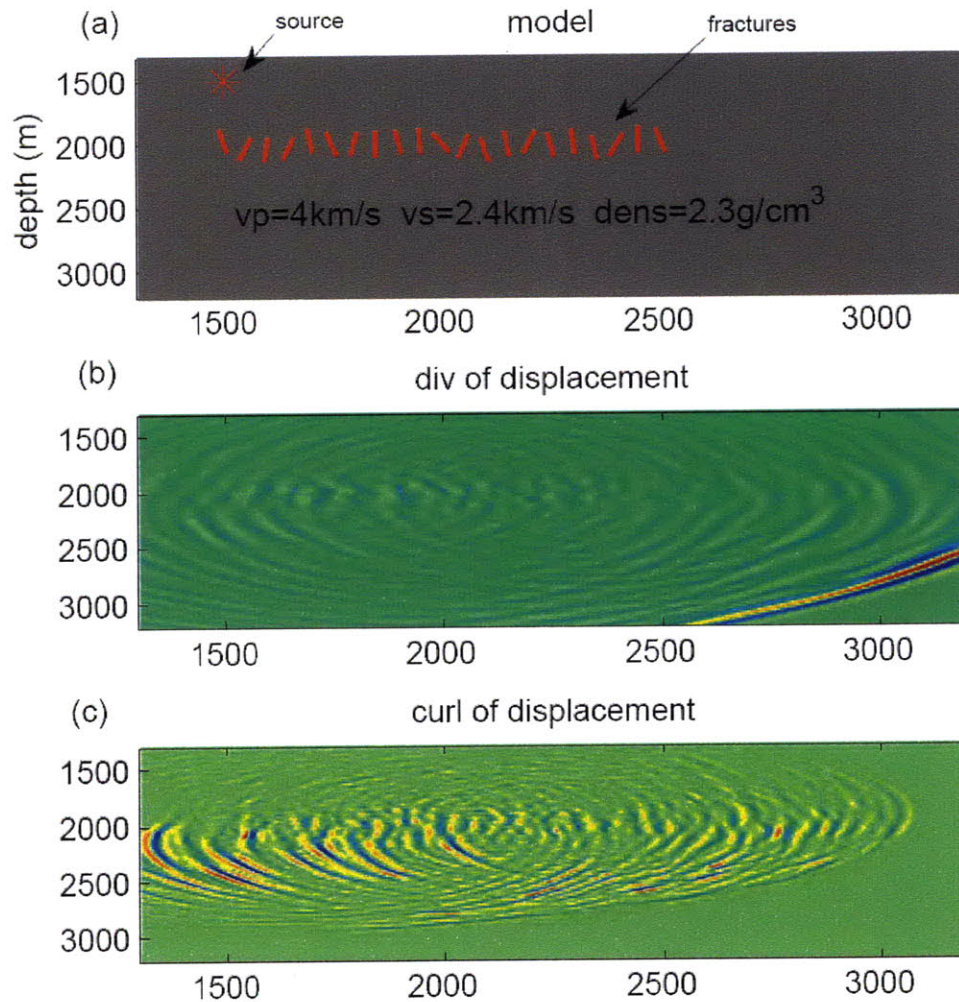


Figure 3.2.2: (a) is a homogeneous isotropic model with 21 non-parallel fractures, red lines indicate fractures and asterisk is the source. Parameters for the background medium are shown in (a) and fractures' normal and tangential compliances are $0.5 \times 10^{-9} \text{m/Pa}$ and 10^{-9}m/Pa , fracture length is 200m, the source wavelet is a Ricker wavelet with 40Hz central frequency; (b) and (c) show snapshots of the divergence and curl of the scattered wave field at 0.54s.

3.2.2 Scattering strength

For a given frequency, scattering strength is defined as the maximum of the fracture response function over all radiation angles, so it is frequency dependent. Figure 3.2.3 shows the scattering strength of P-to-P scattering for fractures having different tangential compliances

and different compliance ratios. We find that usually P-to-P scattering is stronger at small incident angle except for the case of a small compliance ratio (~ 0.1). Figure 3.2.4 shows the corresponding P-to-S scattering strength where regardless of the variation of compliance ratio, P-to-S scattering is always strongest near 40° incident angle.

By comparing P-to-P and P-to-S scattering strength in figures 3.2.3 and 3.2.4, we can find that, for most cases, P-to-S scattering is stronger than P-to-P scattering when the compliance ratio is smaller than 1. For both P-to-P and P-to-S scattering, the scattering strength will increase about 2 orders when the compliance increases 1 order, and P-to-P scattering is more sensitive to the change of normal compliance, while P-to-S scattering is more sensitive to the change of tangential compliance.

If the compliance ratio Z_N/Z_T is ≤ 0.5 (as discussed in section 2.3), then, generally, P-to-S scattering would be stronger than P-to-P scattering when the incident angle is larger than 20° . This implies that it might be easier to detect P-to-S scattered waves at the surface, although it might be hard to analyze such waves because of their complex ray paths.

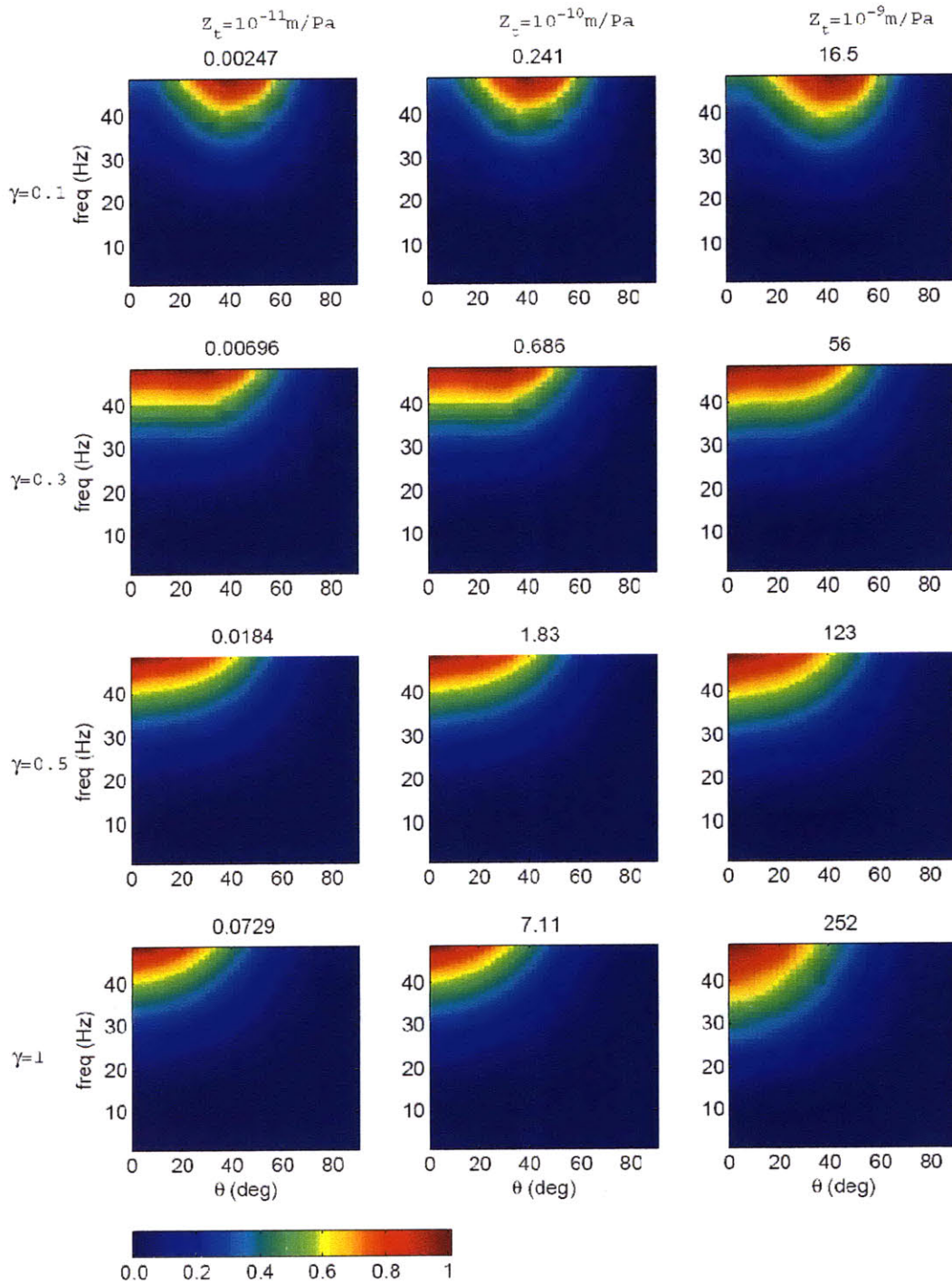


Figure 3.2.3: P-to-P scattering strength for different tangential compliance and different compliance ratio. Horizontal and vertical axes are angle of incidence and frequency. Tangential compliances are 10^{-11} m/Pa, 10^{-10} m/Pa and 10^{-9} m/Pa for the 1st, 2nd and 3rd column, respectively. And the compliance ratios are 0.1, 0.5 and 1 for the 1st, 2nd and 3rd row,

respectively. The scattering strength for each panel is normalized to 1 in plotting, the number above each panel is the scaled factor (maximum scattering strength).

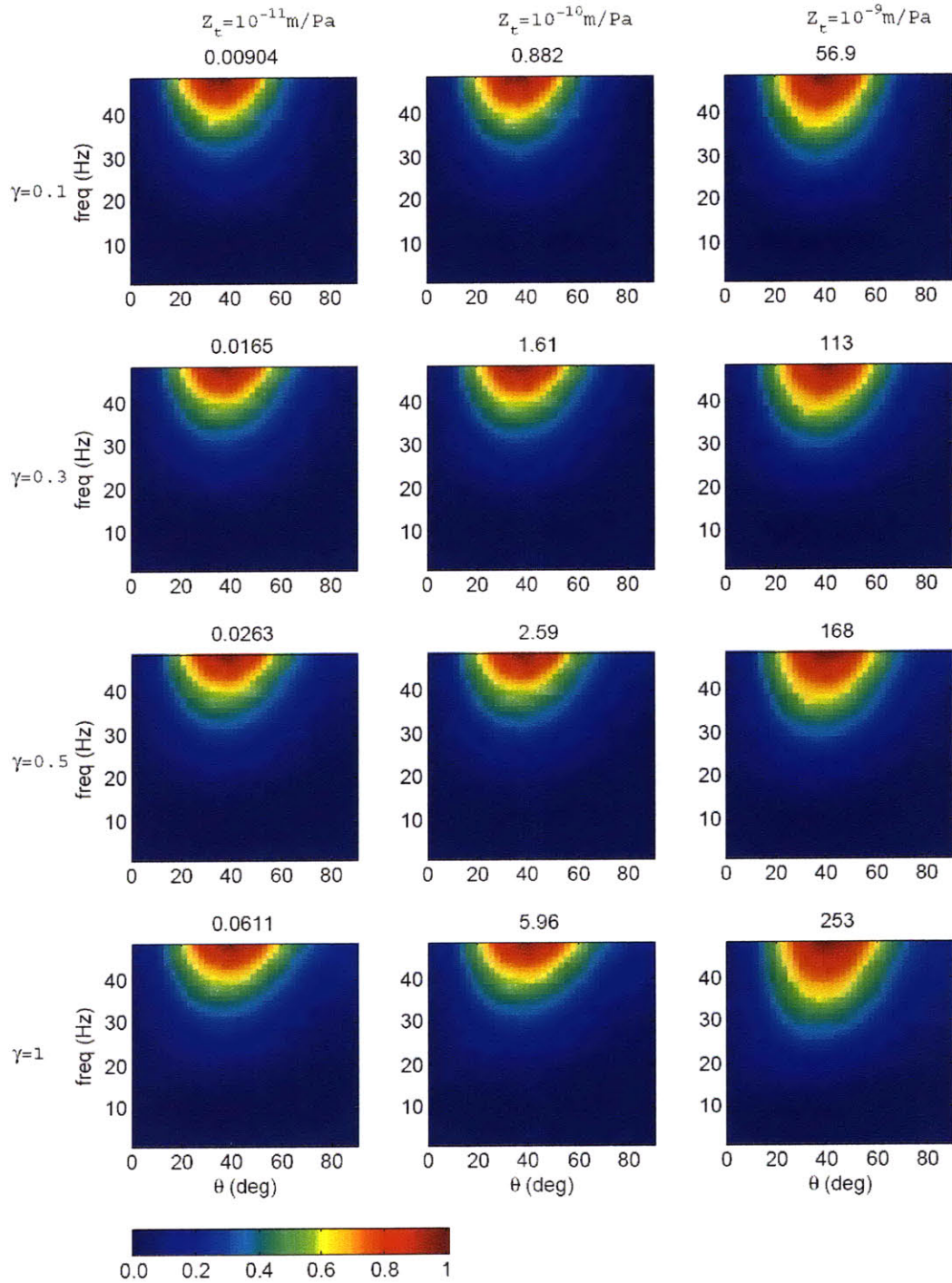


Figure 3.2.4: P-to-S scattering strength for different tangential compliance and different compliance ratio. Horizontal and vertical axes are angle of incidence and frequency.

3.2.3 The effect of matrix Poisson's ratio on fracture scattering pattern

Figure 3.2.5 shows P-to-P and P-to-S scattering patterns for different matrix Poisson's ratio and different compliance magnitudes. When Poisson's ratio increases from 0.2 to 0.3, the scattering patterns change, while scattering strength does not change too much, implying that the scattering strength is less sensitive to the background matrix. Although we only show cases of 50° incidence and compliance ratio equal to 0.5, we can get the same conclusion from all other examples.

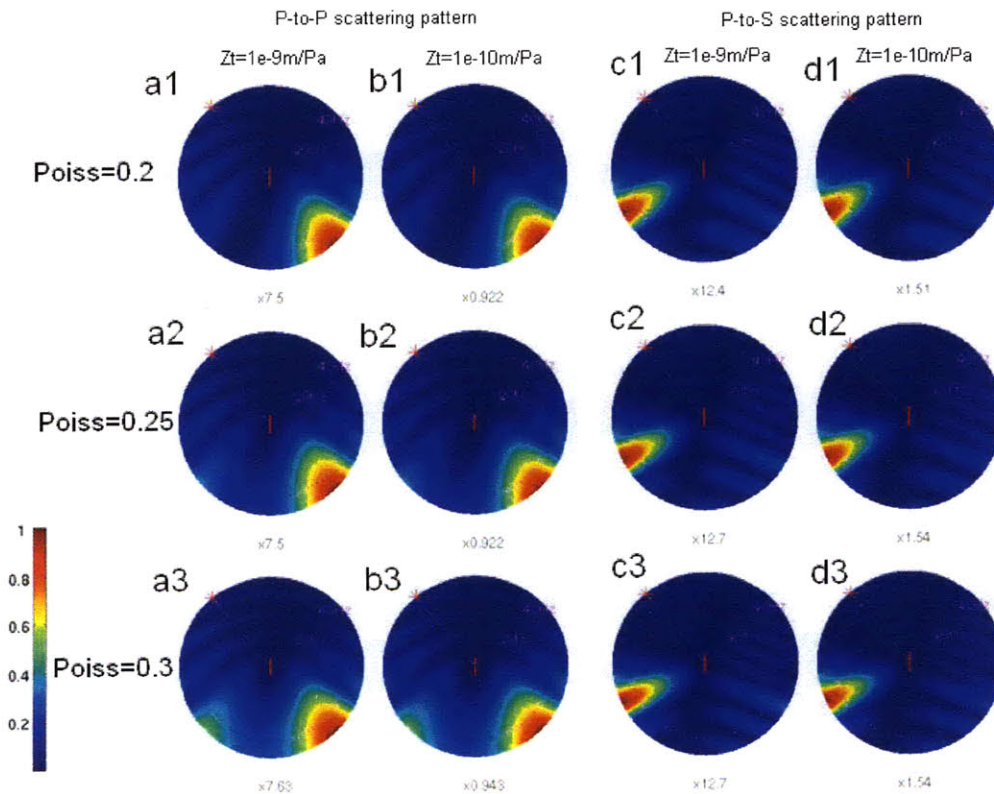


Figure 3.2.5: P-to-P (a and b columns) and P-to-S (c and d columns) scattering patterns for different matrix Poisson's ratio. Poisson's ratios are shown on left most of each row, and tangential compliances are shown on top of each column. In these examples, matrix P-wave velocity is fixed to 4km/s, while S-wave velocity is changed to get models with different matrix Poisson's ratio. Incident angle is 50° and the compliance ratio is 0.5 for all examples.

3.2.4 The effect of fracture length on fracture scattering

Table 3.2.3 shows the P-to-P and P-to-S scattering for models with two different fracture lengths at different incident angles. The incident wavelength is the same for both fracture models. From Table 3.2.3, we can see that the dominant scattering directions of the two fracture models with different fracture lengths are very similar, but both the P-to-P and P-to-S radiation patterns for the 100m long fracture has a broader distribution of high amplitude regions. From this comparison, we see that the scattering of a fracture will approach that of the scattering from a point scatterer when the length of the fracture decreases. We also can find that the scattering strength increases with the increasing fracture length.

		P-to-P scattering		P-to-S scattering	
FracL θ_{inc}		100 m	200 m	100 m	200 m
	0°				
		1.56	2.76	0.572	0.683
30°					
		1.23	2.23	1.46	2.37

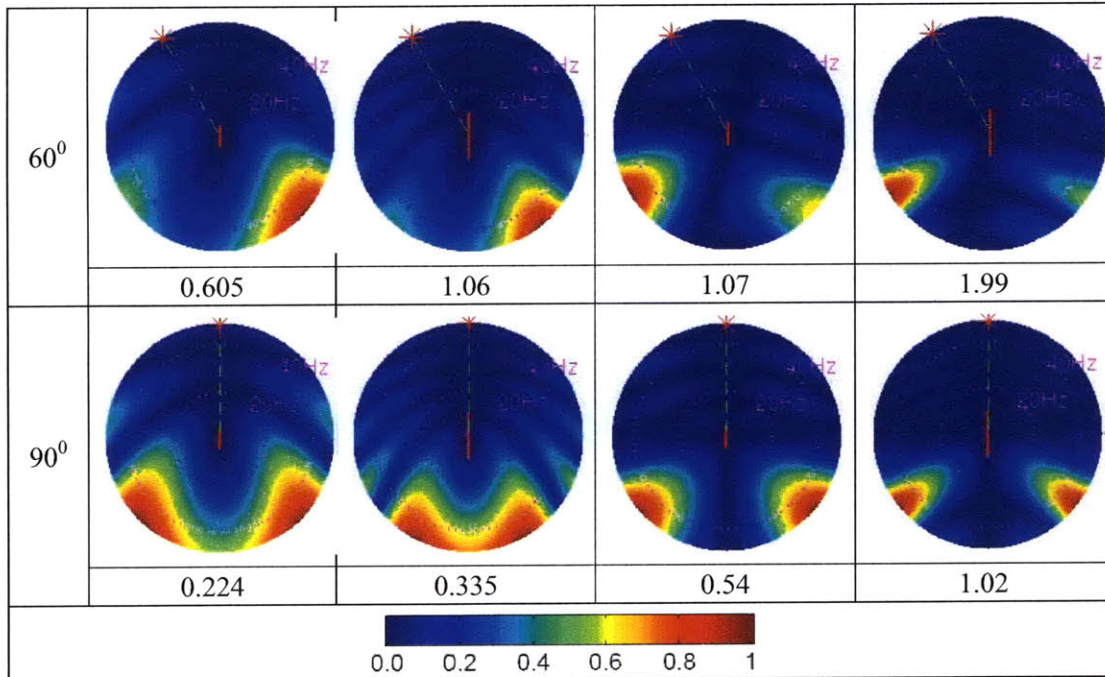


Table 3.2.3: $F_{pp}(\theta, \omega)$ and $F_{ps}(\theta, \omega)$ of two fracture models with different fracture lengths. The two left columns show $F_{pp}(\theta, \omega)$ of different incident angles, and the fracture length is 100m and 200m for the 1st column and 2nd column, respectively. The two right columns show the corresponding $F_{ps}(\theta, \omega)$. The normal and tangential compliance of these models are 10^{-10} m/Pa, matrix P-wave and S-wave velocities are 4 km/s and 2.4 km/s, density is 2.3 g/cm³, and the source wavelet is Ricker wavelet with 40 Hz central frequency

3.3 Suggestions on Field Data Processing

Based on our numerical study, we found that, if Z_N/Z_T is ≤ 0.5 , then we will detect stronger P-to-S fracture scattering energy in the field, and fractures would generate the strongest P-to-S scattering when the incident wave is about $40^\circ - 50^\circ$ to the normal of fracture planes. Most of the P-to-S fracture scattering is back in the direction towards the source but downward. From both synthetic data and field data analysis, Willis (2006) found that stacking of data collected in different azimuthal angles can significantly enhance the signal-to-noise of P-to-P fracture scattered waves. However, traditional stacking is not acceptable for P-to-S fracture scattered waves, because, for a given source–receiver pair, the scattering point is not located at the center of the raypath between the source and receiver, the ray paths for P-to-S

scattered waves are much more complicated. So, if we want to use P-to-S fracture scattered waves for fracture characterization, we can either use pre-stack data or develop a more sophisticated P-to-S stacking scheme.

Fracture compliance value is important for estimating fluid flow properties. We can detect the ratio of Z_N/Z_T from radiation pattern and absolute value of compliance from scattering strength if radiation pattern and scattering strength could be measured. However, as we discussed previously, fracture scattered waves are contaminated by the reflectivity of the matrix reflectors below the fracture zone, so an accurate velocity model of the field is needed to obtain the correct fracture compliance value.

Chapter 4

Conclusions

We studied scattering from single fracture using numerical modeling and found the characteristics of fracture P-to-P and P-to-S scattering, which will aid in fracture characterization. Due to the gravity of overburden and regional stress field, fractures are usually close to vertical in a fractured reservoir, and the source is normally located at the surface, thus most of the fracture scattering energy will propagate downwards, specifically, the P-to-P scattering energy propagates down and forward while the P-to-S scattering energy propagates down and backward. Therefore, for a vertical fracture system, most of the fracture scattered waves observed on the surface are, first scattered by fractures, and then reflected back to the surface by reflectors below the fracture zone, so the fracture scattered waves have complex ray paths and are contaminated by the reflectivity of structure's reflectors. Because of the complexity of the recorded seismic signals, instead of using traditional migration or inversion methods, we intend to develop a statistical method for fracture characterization.

In this paper, we only show the 2D study, but our work will move to 3D to see the comprehensive seismic response of a finite fracture. The single fracture study will greatly increase our knowledge of fracture scattering and help us to understand the complex response of a fracture network.

Bibliography

- Aki, K., 1992. Scattering conversions P to S versus S to P, *BSSA* **82**, no. 4, 1969-1972.
- Burns, D.R., Willis, M.E., and Toksoz, M.N., 2007. Fracture properties from seismic scattering, *The Leading Edge* **26**, no.9, 1186-1196.
- Coates, R.T. and M. Schoenberg, 1995. Finite-difference modeling of faults and fractures, *Geophysics* **60**, no. 5, 1514-1526.
- Daley, T.M., K. Nihei, E. Myer, J. Queen, M. Fortuna, J. Murphy, and R. Coates, 2002. Numerical modeling of scattering from discrete fracture zones in a San Juan Basin gas reservoir, *72nd Annual International Meeting, SEG, Expanded Abstracts*, 109-112.
- Grechka, V. and M. Kachanov, 2006. Effective elasticity of fractured rocks: A snapshot of the work in progress, *Geophysics* **71**, no. 6, W45-W58.
- Grechka, V., 2007. Multiple cracks in VTI rocks: Effective properties and fracture characterization, *Geophysics* **72**, no. 5, D81-D91.
- Groenenboom, J., and J. Falk, 2000. Scattering by hydraulic fractures: Finite-difference modeling and laboratory data, *Geophysics* **65**, no. 2, 612-622.
- Gu, B., R. Suarez-Rivera, K.T. Nihei and L.R. Myer, 1996. Incidence of plane waves upon a fracture, *J. Geophys. Res.* **101**, no. B11, 25337-25346.
- Gurevich, B., D. Makarynska and M. Pervukhina, 2009. Are penny-shaped cracks a good model for compliant porosity, *79th Annual International Meeting, SEG, Expanded Abstracts*, 3431-3435.
- Hardin, E.L., and C.H. Cheng, 1987. Fracture characterization by means of attenuation and generation of tube waves in fractured crystalline rock at mirror lake, New Hampshire, *JGR.* **92**, no. B8, 7989-8006.

- Hudson, J.A., 1991. Overall properties of heterogeneous material, *Geophys. J. Int.* **107**, 505-511.
- Hsu, C.J., and M. Schoenberg, 1993. Elastic waves through a simulated fractured medium, *Geophysics* **58**, no. 7, 964-977.
- Kachanov, M., 1992. Effective elastic properties of cracked solids: critical review of some basic concepts, *Appl. Mech. Rev.* **45**, no. 8, 304-335.
- Lu, C.P., D. Wang, M. Johns and et al., 2009. A field study of azimuthal seismic anisotropy in fractured carbonates at Canyon Lake, central Texas, *The Leading Edge*, 1322-1332.
- Lubbe, R., J. Sothcott, M.H. Worthington and C. McCann, 2008. Laboratory estimates of normal and shear fracture compliance, *Geophysical Prospecting* **56**, 239-247.
- Lubbe, R. and M.H. Worthington, 2006. A field investigation of fracture compliance, *Geophysical Prospecting* **54**, 319-331.
- Majer, E., Peterson, J., Daley, T., Kaelin, B., Myer, L., Queen, J., D'Onfro, P., Rizer, W., 1997. Fracture detection using crosswell and single well surveys, *Geophysics* **62**, no. 2, 495-504.
- Pyrak-Nolte, L. and N. G.W. Cook, 1987. Elastic interface waves along a fracture, *Geophysical Research Letters* **14**, no. 11, 1107-1110.
- Pyrak-Nolte, L., L.R. Myer, and N. G.W. Cook, 1990. Transmission of seismic waves across single natural fractures, *Journal of Geophysical Research* **95**, no. B6, 8617-8638.
- Pyrak-Nolte, L., J. Xu, and G.M. Haley, 1992. Elastic interface waves propagating in a fracture, *Physical Review Letters* **68**, no. 24, 3650-3653.

- Pyrak-Nolte, L., S. Roy, B.L. Mullenbach, 1996. Interface waves propagated along a fracture, *Journal of Applied Geophysics* **35**, 79-87.
- Pyrak-Nolte, L., L.R. Mye, 1999. Single fractures under normal stress: the relation between fracture specific stiffness and fluid flow, *Int. J. of Rock Mech. And Min. Sci* **37**, 245-262.
- Schoenberg, M., 1980. Elastic wave behavior across linear slip interfaces, *J. Acoust. Soc. Am.* **68**, no. 5, 1516-1521.
- Schoenberg, M. and C.M. Sayers, 1995. Seismic anisotropy of fractured rock, *Geophysics* **60**, no. 1, 204-211.
- Sanchez-Sesma, F.J. and U. Iturraran-Viveros, 2001. Scattering and diffraction of SH waves by a finite crack: an analytical solution, *Geophys. J. Int.* **145**, 749-758.
- Sayers, C.M., 2009. Seismic characterization of reservoirs containing multiple fracture sets, *Geophysical Prospecting* **57**, 187-192.
- Sayers, C.M., A.D. Taleghani and J. Adachi, 2009. The effect of mineralization on the ratio of normal to tangential compliance of fractures, *Geophysical Prospecting* **57**, 439-446.
- Vetri, L., E. Loinger, J. Gaiser, A. Grandi, H. Lynn, 2003. 3D/4C Emilio: Azimuth processing and anisotropy analysis in a fractured carbonate reservoir, *The Leading Edge*, 675-679.
- Willis, M. E., D. Burns, R. Rao, B. Minsley, M.N. Toksoz, and L. Vetri, 2006. Spatial orientation and distribution of reservoir fractures from scattered seismic energy, *Geophysics* **71**, no. 5, O43-O51.
- Worthington, M.H. and J. Hudson, 2000. Fault properties from seismic Q, *Geophys. J. Int* **143**, 937-944.
- Worthington, M.H. and R. Lubbe, 2007. The scaling of fracture compliance, *Geological Society, London, Special Publications* **270**, 73-82.